



Research article

Quantification of polystyrene microsphere attachment probability at the oil–water interface using a microfluidic platform

In Hwan Jung^a, Kyu Hwan Choi^{a,1}, Tae Seok Seo^{a,**}, Hyosung An^{b,***},
Bum Jun Park^{a,*}

^a Department of Chemical Engineering (BK21 FOUR Integrated Engineering Program), Kyung Hee University, Yongin, Gyeonggi-do, 17104, South Korea

^b Department of Petrochemical Materials Engineering, Chonnam National University, Yeosu, Jeollanam-do, 59631, South Korea

ARTICLE INFO

Keywords:

Colloid
Interface
Interparticle interactions
Wettability
Interface-adsorption efficacy

ABSTRACT

This study investigates the effects of interparticle interactions and wettability on the particle attachment efficacy to the oil–water interface. Three types of PS particles with different surface functional groups were examined at varying salt concentrations and the number of particles injected into the interface. Based on the microfluidic method and the surface coverage measurement, we found that the two contributing factors significantly influenced particle attachment efficiency to the interface, while the wettability factor has a major contribution. This research contributes to the understanding of physicochemical aspects of particle assembly at fluid interfaces and can offer strategies for forming tailored structures with desired interfacial properties.

1. Introduction

Particle-laden interfaces are extensively utilized in numerous applications ranging from food and pharmaceuticals to cosmetics and enhanced oil recovery [1–14]. The binding of colloidal particles to a fluid–fluid interface reduces the interfacial energy, leading to the stabilization of the interface against coalescence [15,16]. When a particle-laden fluid interface is formed, two types of interparticle forces, the electrostatic dipolar force, and the local interface deformation-induced capillary force, become unusually strong and compete with each other, resulting in unique assembly microstructures [17–21]. Generally, charged spherical particles under low electrolyte conditions are governed by the electrostatic repulsive force, whereas nonspherical particles under low electrolyte conditions or spherical particles under high electrolyte conditions are dominated by the attractive capillary force [22–33]. Furthermore, the surface free energy associated with the attachment of particles to fluid–fluid interfaces is influenced by several factors, such as the chemical nature, size, roughness, and wettability of particles [34–36].

Over the past 30 years, extensive experimental and theoretical studies have been conducted to investigate various aspects of colloidal particles at fluid–fluid interfaces, including the configurations of isolated particles, electrostatic and capillary interactions between interface-trapped particles, interaction heterogeneity, assembly behaviors and microstructures, interface rheological

* Corresponding author.

** Corresponding author.

*** Corresponding author.

E-mail addresses: seots@khu.ac.kr (T.S. Seo), hyosungan@jnu.ac.kr (H. An), bjpark@khu.ac.kr (B.J. Park).

¹ Current address: Department of Chemical Engineering, University of California Santa Barbara, Santa Barbara, CA 93106, USA.

<https://doi.org/10.1016/j.heliyon.2023.e16588>

Received 10 March 2023; Received in revised form 8 May 2023; Accepted 22 May 2023

Available online 26 May 2023

2405-8440/© 2023 The Authors. Published by Elsevier Ltd. This is an open access article under the CC BY-NC-ND license (<http://creativecommons.org/licenses/by-nc-nd/4.0/>).

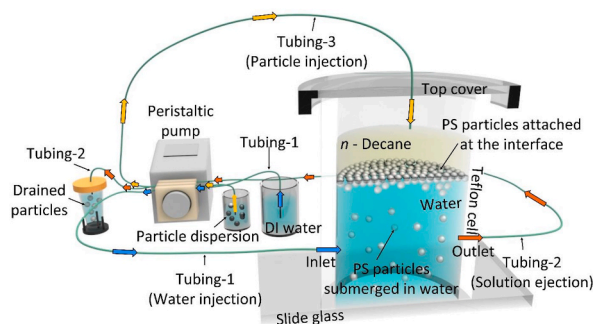


Fig. 1. Schematic experimental setup for determining the particle attachment probability using the microfluidic platform (not drawn to scale).

properties, and Pickering emulsion stability [37–41]. Note that these interfacial properties of colloidal particles are related to two crucial factors - wettability and interparticle interactions. Wettability is determined by the three-phase contact angle θ_c at a fluid–fluid interface, which represents the partition of particles between the two fluid phases. The wettability of charged microspheres at the interface can directly affect their electrostatic interactions [18,26,42–44]. Asymmetric surface charge dissociation across the interface can alter the magnitude of an electric dipole, which in turn depends on the relative position of particles at the interface. It should be noted that electric dipole-induced long-range repulsive interactions play a key role in determining the microstructural properties of particle-laden interfaces [15,33,45]. Despite the close relationship between wettability and interparticle interactions, there have been very few efforts to understand their relative effects on the formation of particle-laden fluid interfaces, especially regarding the probability of particle attachment to the interface. Additionally, there is a lack of systematic studies on the efficiency of particle adsorption to the interface at a large scale.

In this study, we investigated the relative contributions of particle wettability and interparticle interactions to the attachment probability of colloidal microspheres to an oil–water interface, given by

$$P_{att} = \frac{N_I}{N_{tot}} \quad (1)$$

where N_{tot} is the total number of particles added and N_I is the number of particles attached to the interface. To quantitatively measure P_{att} at the interface, we developed a microfluidic platform system that efficiently handles a large number of particles. Additionally, we conducted surface coverage analysis by adding a relatively small number of particles to the interface and compared the results with those obtained from the microfluidic system. We evaluated three types of polystyrene (PS) particles with different surface functionalities and wettabilities, namely carboxyl PS (CPS), sulfonate PS (SPS), and amidine PS (APS). Interparticle interactions at the oil–water interface were directly measured using optical laser tweezers [24,46,47], and the three-phase contact angles of the particles at the interface were determined using the gel trapping method [48].

2. Materials and methods

2.1. Materials

CPS (4% w/v), SPS (8% w/v), and APS (4% w/v) were purchased from Thermo Fisher Scientific. Deionized (DI) water (resistivity $\geq 18.2 \text{ M}\Omega\cdot\text{cm}$, Aquapuri5, Youngin, Korea) and *n*-decane (99+%, Acros Organics, USA) were used as aqueous and oil phases, respectively, to form an oil–water interface. Prior to usage, *n*-decane was filtered with aluminum oxide particles (Al_2O_3 , Pore size = 58 Å, Sigma-Aldrich, USA) to eliminate any polar contaminants. 2-Propanol (IPA, anhydrous 99.5%, Sigma-Aldrich) was utilized as a solvent to spread particles at the oil–water interface. NaCl (99.0%) was obtained from Samchun, Korea. Chemicals and solvents were used without any further purification unless specified.

2.2. Microfluidic platform for determining P_{att}

A flow cell was utilized in conjunction with a microfluidic system (Fig. 1) to investigate the particle attachment probability at the oil–water interface. Slide glass (32 mm \times 76 mm, Matsunami Glass Ind, Japan) was attached to a Teflon hollow cylinder (diameter of 21 mm and height of 40 mm). Low-density polyethylene tubes (0.034" ID, Scientific Commodities, Inc, USA) were connected to the flow cell as an inlet and outlet for continuous injection and ejection of the aqueous phase. A peristaltic pump (ISMATEC, USA) with three channels was used to regulate the flow rates of the inlet and outlet. To form the oil–water interface, 8 mL DI water and 2 mL *n*-decane were gently added to the flow cell using a micropipette. Through tube-3, which was connected to a top cover, as shown in Fig. 1 and 0.6 mL of the particle suspension (4.5 g/L with IPA/particle solution = 1:4 v/v) was slowly dropped onto the surface of the *n*-decane phase at a rate of 0.31 mL/min, where IPA was used as a spreading solvent [45]. Upon the addition of the particle solution to the flow cell, some PS particles were attached to the oil–water interface, and others were submerged in the aqueous phase. During the experiment, the aqueous phase was gently stirred with a magnetic stirring bar at 150 revolutions per minute (rpm) to ensure that the

water-immersed particles were dispersed and drained. This slow agitation likely minimized the flow-induced detachment of already attached particles. To collect the unattached particles dispersed in the aqueous phase, fresh DI water was injected into the flow cell at a rate of 0.4 mL/min through tube-1, and the water phase was simultaneously ejected from tube-2 at the same flow rate. The drained particle solution was collected in a conical tube (50 mL, 30 mm × 115 mm, LK lab, Korea) for 100 min. The collected particle suspension was centrifuged at 3000 rpm for 10 min using a centrifuge (Labogene 416, Labogene, Korea) to remove NaCl. After discarding the supernatant water, the particles were re-dispersed in DI water. This rinsing procedure was repeated twice more. In the final washing step, a portion of the supernatant was removed, and the bottom 10 mL with the particles (hereafter “concentrated particle suspension”) was separated. The optical density (OD at $\lambda = 310$ nm) of the concentrated particle suspension (200 μ L) was measured using a Nanodrop (Synergy™ HTX Multi-Mode Microplate Reader, TECAN, Switzerland). The measured OD value was converted to the particle concentration to determine P_{att} .

2.3. Surface coverage measurements

DI water (4 mL) and *n*-decane (2 mL) were added to a Petri dish (35 × 10 mm, Falcon, USA) to form an oil–water interface [45]. Subsequently, a particle solution (concentration of 0.45 g/L) was carefully added dropwise (100 μ L) onto the oil–water interface. After 10 min, the microstructures of the interface-trapped particles were captured using an inverted microscope (Eclipse Ti, Nikon, Japan) equipped with an objective lens (CFI S Plan Fluor ELWD 20XC, Nikon, Japan) and a charge-coupled device camera (CCD, EOS 700D, Canon, Japan). To minimize the time evolution of colloidal microstructures [45,47], all microscope images were taken within 15 min. To ensure statistically reliable results, 25 images were evaluated under each experimental condition. The average surface coverage σ of the obtained microscopic images was analyzed using Python software. Gaussian filtering was applied, followed by binarization and detection of the particle boundaries. The surface coverage was estimated using the equation $\sigma = \frac{S_p}{S_i}$, where S_p and S_i represent the total area of particle regions and the entire image area, respectively. The number of particles added to the Petri dish was estimated by

$$N_p = \frac{m}{\rho_p V_p} \quad (2)$$

where m denotes the total particle mass added, $\rho_p = 1.055$ g/mL is the particle density, and V_p represents the volume of a single particle.

2.4. Pair interaction measurements

A flow cell was constructed with inner and outer cylinders, as previously reported [24,25,49]. Briefly, the inner hollow cylinder was a Teflon ring (9 mm in height and 12 mm in diameter) attached to the inside of an aluminum ring (8 mm in height and 14 mm in diameter). For the outer cell, a circular coverslip (no. 1.5H, Marienfeld, Germany) was treated with oxygen plasma (PDC-32G-2, Harrick Plasma Inc, USA) and attached to the bottom of a glass hollow cylinder (11 mm in height and 25 mm in diameter) using UV glue (Norland optical adhesive 81, Norland Products Inc, USA). DI water (1.5 mL) was injected into the inner cylinder, followed by gentle addition of *n*-decane (200 μ L). The particle solution, diluted with IPA (volume ratio = 4:1), was carefully added dropwise (20 μ L) onto the surface of the *n*-decane phase. The height of the oil–water interface was adjusted by removing approximately 0.9 mL of water from the gap between the outer and inner cylinders, allowing the oil–water interface to be pinned at the boundary junction between the aluminum and Teflon rings. After 30 min of stabilization, the particle–particle interaction was measured using optical laser tweezers (10 W CW Nd:YAG laser, $\lambda = 1064$ nm, Coherent Matrix, USA) connected with an inverted microscope (Ti-U, Nikon, Japan). The laser beam, passing through a water immersion objective lens (CFI Plan Apochromat VC 60, NA = 1.2, Nikon, Japan), was highly focused on a focal plane, resulting in an optical trap [25,47,49]. An acousto-optic deflector (Opto-electric DTSXY-400-1064, OPTO-ELECTRONIC, France) was used to generate multiple traps, and trap positions were individually controlled using the LabVIEW software. To measure the pair interaction force, two particles were trapped at the oil–water interface, and one particle was translated stepwise towards the other stationary particle. A sequence of optical microscope images was recorded at a rate of 30 frames per second using a CCD camera (KP-M1AN, Hitachi, Japan). The images were analyzed using ImageJ software [50] to calculate the displacement, Δx , of the stationary particle from its equilibrium position and the separation, r , between the two particles. The interparticle force as a function of r was determined using

$$F_{\text{trap}}(r) = \kappa_t \Delta x(r) \quad (3)$$

where the trap stiffness κ_t was obtained using the drag calibration method [47,51].

2.5. Three-phase contact angle measurements

The three-phase contact angle of a colloidal particle at the oil–water interface was determined using the gel trapping method [48]. A 2 wt% phytigel (Sigma-Aldrich) aqueous solution was heated to 80°C–90°C using a water bath. The melted phytigel solution (2 mL) was transferred into a Petri dish (Φ 35 mm × 10 mm, Corning, USA), which was placed in a 60°C oven. Preheated *n*-decane at 60°C was added to the top of the phytigel solution. A colloidal particle suspension (IPA/particle solution = 7:3 v/v) was gently dropped onto the surface of the oil phase using a micropipette. After 3 min, the sample was cooled down to room temperature for 5 min, resulting in the aqueous subphase forming a gel. The oil phase was carefully removed using a micropipette. In separate glassware,

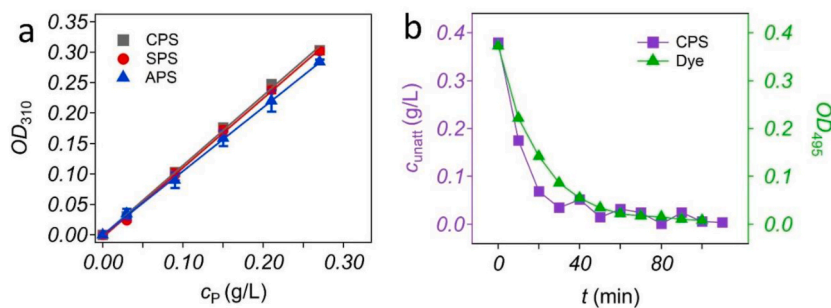


Fig. 2. Optimization of the microfluidic system. (a) Calibration curves of OD₃₁₀ versus c_p using UV-Vis spectroscopy measurements. (b) Determination of optimal water replacement time t for performing the microfluidic experiment.

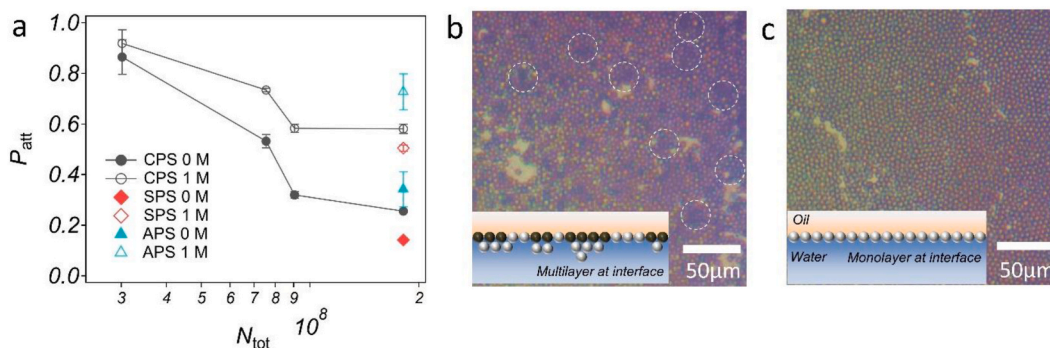


Fig. 3. Measurements of P_{att} at oil-water interface using the microfluidic system. (a) Plot of P_{att} versus N_{tot} . (b,c) Example optical microscope images showing the multilayered regions (b) and the monolayered regions (c) at $N_{tot} = 9 \times 10^7$ and $c_{NaCl} = 1$ M. Locally darker regions indicated by the dotted circles in panel b represent some of the multilayered regions. Insets are the corresponding prospective schematics.

polydimethylsiloxane (PDMS, Sylgard 184A, Sewang Hitech, Korea) was mixed with a curing agent (Sylgard 184B, Sewang Hitech, Korea) at a mass ratio of 10:1. The mixture was introduced onto the surface of the phytigel and cured for 2 days. The cured PDMS slab was peeled off and washed with DI water. The PDMS containing the particles was platinum-coated using a plasma coater (Seron Technology, Korea), and the three-phase contact angle of the particles was measured by scanning electron microscopy (SEM, AIS-2100, Seron Technology).

3. Results and discussion

3.1. Optimization of the microfluidic system

The microfluidic system (Fig. 1) was optimized before use to systematically evaluate P_{att} . An excess number of particles N_{tot} were added to the oil-water interface formed in the flow cell. Some PS particles became adsorbed to the oil-water interface, whereas others were submerged in the aqueous phase. The adsorbed particles were considered “attached”, and the submerged particles were labeled “unattached”. The particle concentration $c_p = c_{unatt}$ in the aqueous phase (“unattached” particles) was measured to estimate the number of unattached particles N_{unatt} and the number of interface-attached particles,

$$N_{att} = N_{tot} - N_{unatt} \quad (4)$$

To obtain a calibration curve that determines N_{unatt} , UV-Vis spectroscopy was used to measure the optical density (OD₃₁₀) of particle suspensions with known particle concentrations c_p . The solid lines in Fig. 2a indicate linear regression, yielding slopes of 1.148 ± 0.013 , 1.123 ± 0.012 , and 1.050 ± 0.007 for CPS, SPS, and APS, respectively, with all of $R^2 \geq 0.999$. This calibration curve of OD₃₁₀ versus c_p was used to convert the measured OD value to $c_p = c_{unatt}$ and thus P_{att} during the microfluidic experiment. Additionally, the water replacement time t was optimized to ensure that all existing particles in the aqueous phase were drained and collected completely. To achieve this, fresh water was injected into the flow cell at a rate of 0.4 mL/min and ejected at the same rate for a given t . The particle suspension was then collected into a container and washed, and the OD₃₁₀ was measured using the protocol described in the experimental section. The obtained OD₃₁₀ value was converted to $c_p = c_{unatt}$ using the calibration curve in Fig. 2a. These procedures were repeated with varying t to determine the optimal water replacement time to completely collect the water-immersed particles that were unattached to the oil-water interface. Furthermore, a similar experiment was conducted with rhodamine 110 without adding

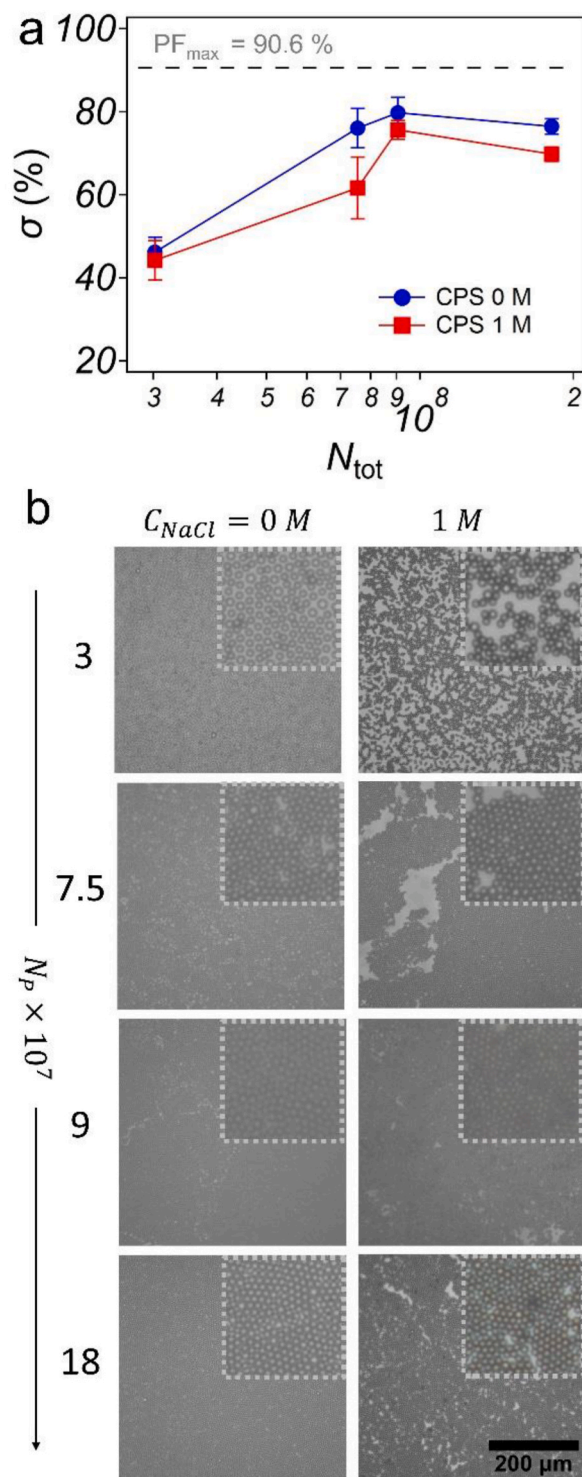


Fig. 4. Evaluation of σ depending on N_{tot} and c_{NaCl} . (a) Plot of σ versus N_{tot} . PF_{max} denotes the maximum packing fraction for spherical particles with a two-dimensional monolayer [52]. (b) Representative optical microscope images showing microstructures of interface-trapped particles. The insets are the magnified images.

particles, and the optical density at 495 nm (OD_{495}) was measured. As shown in Fig. 2b, the measured c_{unatt} in the presence of particles and OD_{495} with rhodamine 110 consistently approached zero at $t \gtrsim 80$ min, indicating that all components initially contained in the flow cell were completely drained. Therefore, a water replacement time of $t = 100$ min was used for further particle attachment

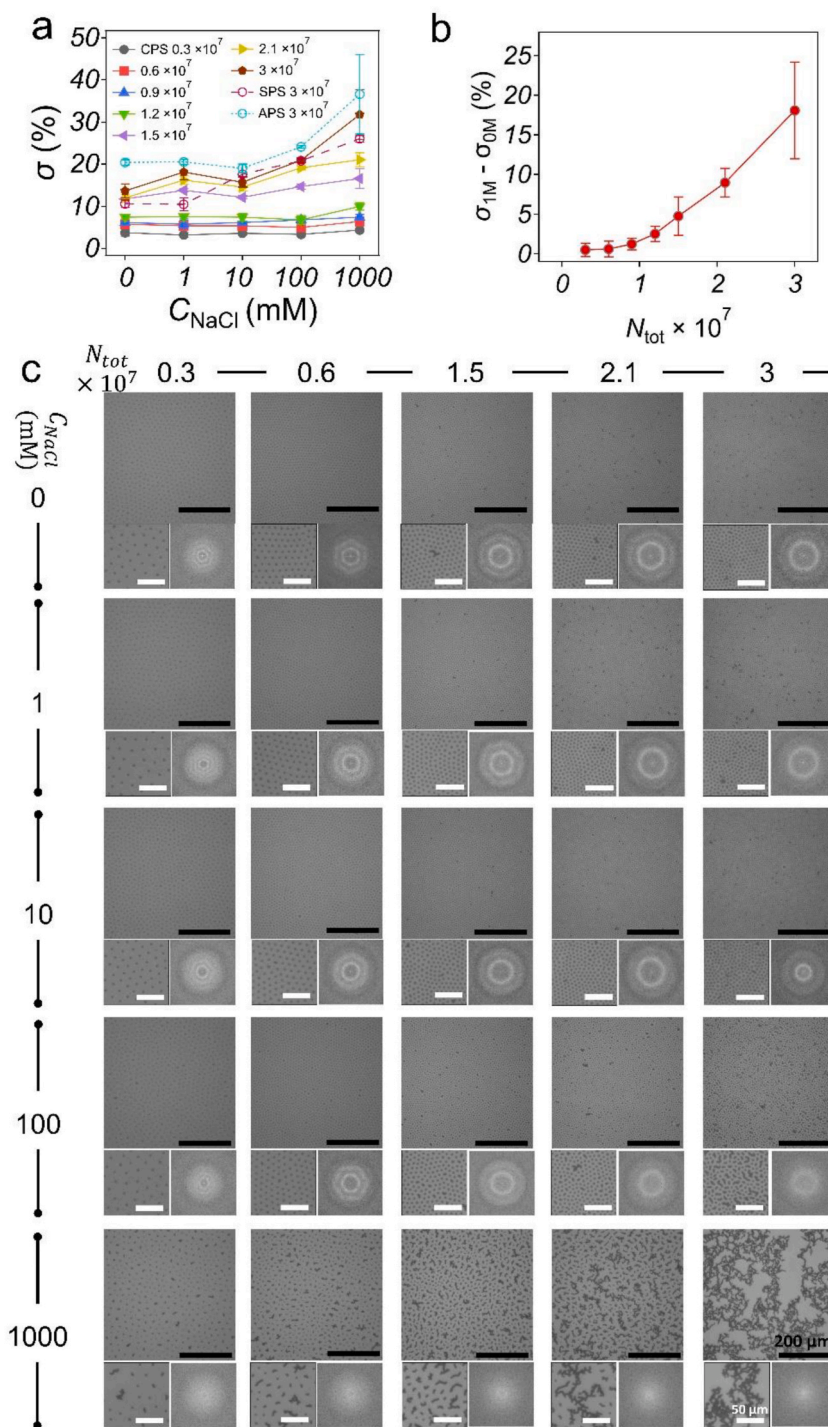


Fig. 5. Effect of c_{NaCl} on interface adsorption for three different PS particles (i.e., CPS, SPS, and APS) through surface coverage measurements. (a) Average surface coverage as a function of c_{NaCl} and N_{tot} . (b) Difference in surface coverage at $c_{NaCl} = 0$ and 1 M as a function of N_{tot} (CPS). (c) Representative optical microscopic images, magnified images, and FFT images showing the microstructures of interface-attached CPS particles depending on c_{NaCl} and N_{tot} .

experiments.

3.2. Quantification of P_{att} to the oil–water interface using the microfluidic system

P_{att} of colloidal particles at the oil–water interface was quantitatively measured for CPS, SPS, and APS at different NaCl concentrations ($c_{NaCl} = 0$ and 1 M) using the microfluidic system, which could efficiently handle a large number of particles (e.g., $N_{tot} \geq 3 \times 10^7$). The presence of NaCl reduces the electrostatic dipole-dipole repulsion between particles at fluid–fluid interfaces, leading to the dominance of capillary forces caused by local interface deformation [26,30,31,46,47]. This results in a structural transformation from long-range ordered hexagonal patterns to aggregated microstructures as c_{NaCl} increases [45,46]. In the case of micrometer-sized spherical particles, the primary cause of interface deformation is known to be the undulation of the three-phase contact line on the particle surface, which leads to quadrupolar capillary attraction [31]. Each data point in Fig. 3a represents the average of two independent runs of the experiment. For CPS, the addition of $N_{tot} = 3 \times 10^7$ at 1 M resulted in slightly higher P_{att} compared to that at 0 M. Such a high salt concentration reduces electrostatic repulsion, leading to the domination of capillary attraction and the formation of aggregated microstructures [45,46]. These microstructures create more free space for additional particle attachment. As N_{tot} increased to $N_{tot} = 9 \times 10^7$ at both $c_{NaCl} = 0$ and 1 M, P_{att} tended to decrease, suggesting a reduction in free interface area for particle adsorption. In other words, as the interface became increasingly saturated with particles, N_{att} did not significantly change despite more particles being added to the interface, resulting in a decrease in P_{att} , which is the ratio of N_{att} to N_{tot} . In contrast, P_{att} at $c_{NaCl} = 1$ M when $N_{tot} = 9 \times 10^7$ and 18×10^7 barely changed. This could be explained by the formation of multilayer particles around the oil–water interface, particularly at high c_{NaCl} . We observed locally darker regions in optical microscopic images (Fig. 3b) representing the presence of these multilayered particles, whereas the monolayered regions showed relatively homogenous contrast (Fig. 3c). High c_{NaCl} reduces the electrostatic double-layer repulsion between the water-immersed particles and between the water-immersed particles and interfacial particles, forming particle aggregates in the multilayer. The critical dimensionless ratio for the formation of particle multilayers can be estimated using the ratio of the total number of particles added to the interface per unit area, given by

$$\gamma_{crit} = \frac{\pi a^2 N_{tot}}{S_I} \quad (5)$$

where a is the particle radius and S_I is the interface area. For instance, at the 1 M NaCl condition, the estimated value for the critical dimensionless ratio was approximately $\gamma_{crit} \approx 2.04$ at $N_{tot} = 9 \times 10^7$.

Furthermore, surface coverage experiments were conducted under the same experimental conditions (Fig. 4). The results showed a similar trend, where the surface coverage σ increased from $N_{tot} = 3 \times 10^7$ to 9×10^7 and reached a plateau (or slight decrease) after $N_{tot} = 9 \times 10^7$ at both NaCl concentrations (Fig. 4a), confirming that the interface was saturated by these particles. The formation of aggregated microstructures at the 1 M condition (Fig. 4b) led to relatively lower σ compared to the case of the 0 M condition, thereby resulting in the increased P_{att} after further particle addition. Additionally, for the different types of PS particles, P_{att} consistently decreased as c_{NaCl} increased (Fig. 3a), demonstrating the negative role of electrostatic repulsion in interfacial attachment. It was also found that P_{att} for APS was the highest, followed by CPS, and P_{att} for SPS was the lowest (Fig. 3a), which will be discussed later. The interface diameter (35 mm) in the surface coverage experiment was larger than that in the microfluidic system (21 mm), where $\gamma \approx 0.73 < \gamma_{crit}$, and thus, the potential for the formation of particle multilayers should decrease. Nevertheless, the surface coverage experiments were further performed under lower N_{tot} conditions to evaluate the electrostatic factor on P_{att} .

3.3. Further evaluation of the electrostatic factor on P_{att}

We further evaluated the effect of the electrostatic interactions of PS particles on their adsorption efficacy to the oil–water interface by measuring the surface coverage depending on c_{NaCl} . Similar to the experimental conditions using the microfluidic system, CPS, SPS, and APS particles were studied at $c_{NaCl} = 0$ and 1 M. The highest limit of N_{tot} in this study was 3×10^7 , which was the lowest limit of the microfluidic measurement. In this condition, the value of γ was approximately 0.25, which was ten times lower than $\gamma_{crit} \approx 2.04$. As a result, the particle concentration was barely sufficient to form multilayered particles around the oil–water interface.

Generally, samples with higher c_{NaCl} exhibited a higher particle adsorption tendency to the interface than those with lower c_{NaCl} (Fig. 5a and b), showing good agreement with the result from the microfluidic measurement (Fig. 3a). For example, in the case of the relatively lower number of CPS particles added (i.e., $N_{tot} = 0.3 \times 10^7$), the surface coverages at 0 and 1 M were $\sim 3.76 \pm 0.74\%$ and $\sim 4.29 \pm 0.43\%$, respectively (see the representative images in Fig. 5c). This difference intensified with increasing N_{tot} , as depicted in Fig. 5b. The salt effect exhibited a similar tendency in the tests with SPS and APS (Fig. 5a). The presence of the electrolyte diminished electrostatic dipolar repulsions between the interface-attached particles and reduced the interparticle separations [46,47], increasing the free interface area for additional particle attachment. For instance, at higher salt concentrations (e.g., 1 M), many aggregates and highly percolated microstructures were formed (Fig. 5c) because of the relatively stronger capillary attractions, increasing the free interface space, which was consistent with the previous report [45,46]. Conversely, at lower salt concentrations, the electrostatic repulsion became dominant, and the interparticle separations were increased. In this case, the continued addition of particles to the particle-laden interface is likely to be energetically unfavorable. Fast Fourier Transform (FFT) analyses implemented with ImageJ software were used to visualize the effects of N_{tot} and c_{NaCl} on microstructures, as illustrated in Fig. 5c [50,53]. When the values of N_{tot} and c_{NaCl} were lower, the FFT resulted in hexagonal patterns that corresponded to long-range ordered microstructures. However, in conditions where the values were higher, these patterns vanished, demonstrating the formation of aggregates and percolated networks.

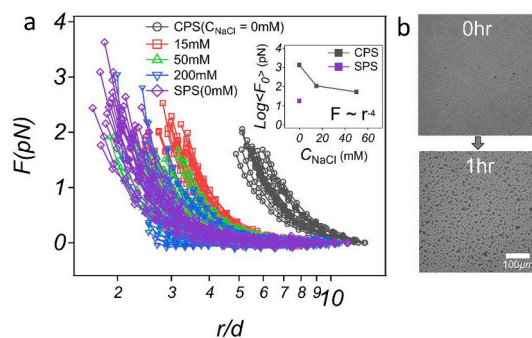


Fig. 6. Evaluation of the electrostatic factor on P_{att} . (a) Measured interaction forces as a function of r/d . The inset shows a logarithmic magnitude of repulsive force $\log \langle F_0 \rangle$ with varying c_{NaCl} . Results of CPS (0 mM) and SPS (0 mM) were obtained from Ref. [24]. (b) Time evolution of microstructures composed of APS particles at oil–water interface (0 mM NaCl). The number of particles added was $N_p = 3 \times 10^7$.

Table 1

Repulsive force magnitude $\langle F_0 \rangle$, zeta potential ζ , three-phase contact angle θ_c , and particle diameter d for CPS, SPS, and APS particles.

Property	CPS ($c_{NaCl} = 0$ mM)	CPS (15 mM)	CPS (50 mM)	CPS (200 mM)	SPS (0 mM)	APS (0 mM)
$\langle F_0 \rangle$ (pN)	1363.96 ^a	108.40	53.28	26.65	18.16 ^a	–
ζ (mV)	-65.6 ± 3.2^a	–	–	–	-57.5 ± 2.2^a	29.8 ± 1.8
θ_c (deg)	142.6 ± 1.2^a	–	–	–	99.4 ± 2.1^a	134.2 ± 1.7
d (μm)	3.16 ± 0.07^a	–	–	–	2.96 ± 0.05^a	2.68 ± 0.03

^a These values were obtained from Ref. [24].

In short, the proportional tendency between P_{att} and c_{NaCl} demonstrates the negative effect of the interparticle electrostatic repulsion on interface attachment. Accordingly, a particle-effective diameter might be introduced; that is, it becomes relatively larger in the presence of stronger repulsive forces, allowing fewer particles to be absorbed into the interface. In addition, the surface coverage for the three types of PS particles increased in the order of SPS, CPS, and APS, showing good agreement with the P_{att} result in Fig. 3a.

3.4. Clarification of relative contributions of interparticle interactions and wettability to P_{att}

To further understand the interface attachment behaviors of the particles depending on the salt concentration, we directly measured the electrostatic interaction force between interface-attached particles using optical laser tweezers (Fig. 6a). Under each salt condition, we repeated the force measurements for more than 18 different particle pairs due to interaction heterogeneity [24]. As depicted in Fig. 6a, for CPS particles, the repulsive force decreased with increasing c_{NaCl} , which was consistent with the previous report [46,47]. The obtained force profiles were fitted using

$$F = F_0 \left(\frac{d}{r} \right)^4, \quad (6)$$

and the mean values of the repulsive force magnitude $\langle F_0 \rangle$ were plotted as a function of c_{NaCl} (inset in Fig. 6a). For CPS particles, the values of $\log \langle F_0 \rangle$ were ~ 3.13 , ~ 2.04 , and ~ 1.43 for 0, 15, and 50 mM, respectively; that is, ~ 50 times stronger repulsion force was obtained with no NaCl ions compared with that at 50 mM. Meanwhile, the force profile at 200 mM did not follow the power law behavior of $F \sim r^{-4}$ due to the weak repulsion and the relatively strong capillary attraction [46].

APS particles at $c_{NaCl} = 0$ mM exhibited a time evolution in their microstructures. The hexagonal pattern of these particles was initially observed, and many aggregates were formed after 1 h (Fig. 6b). This time-dependent aggregate behavior is a typical feature of interfacial particles that carry weak electrostatic repulsions [45]. Accordingly, the weak repulsion of APS particles could be responsible for the highest P_{att} (Fig. 3a) and σ (Fig. 5a), compared with the case of CPS and SPS particles at 0 mM. However, the repulsive force magnitude of SPS particles at $c_{NaCl} = 0$ mM was ~ 75 times weaker than that of CPS particles under the same salt condition, whereas P_{att} and σ for SPS particles exhibited lower P_{att} and σ than those for CPS particles. This observation was likely to be contradictory to the prediction based on the electrostatic repulsion. Therefore, another factor should be involved in interfacial attachment behaviors.

The effect of wettability on particle attachment was examined. CPS particles had a higher contact angle value than SPS particles ($\theta_{c,CPS} = 142.6 \pm 1.2^\circ$ vs. $\theta_{c,SPS} = 99.4 \pm 2.1^\circ$) (Table 1). In other words, more portion of a CPS particle tends to preferentially reside in the oil phase than the case of an SPS particle. When the particle solution with the spreading solvent (IPA) is dropped onto the oil phase, these particles rapidly migrate from the oil phase to the oil–water interface. After these particles reach and hit the interface, the probability of overcoming the interface attachment energy and sinking into the water phase would be lower for hydrophobic particles than for hydrophilic particles. Note that the attachment energy for a spherical particle from the oil phase to the oil–water interface is given by

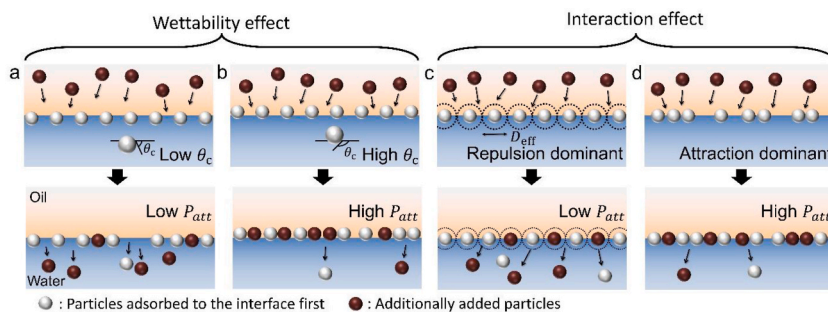


Fig. 7. Schematic illustrations showing the proposed mechanism of particle attachment at oil–water interfaces depending on two factors: wettability and interparticle interactions. (a, b) Wettability effect at low and high θ_c . (c, d) Particle interaction effect at low and high C_{NaCl} . The undulated interface contact line around each particle was not shown for simplicity.

$$\Delta E = -\pi \left(\frac{d}{2}\right)^2 \gamma_{ow} (1 + \cos \theta_c)^2 \quad (7)$$

where γ_{ow} denotes the interfacial tension [37]. Combining the results of the stronger electrostatic repulsion and higher contact angle for CPS than for SPS, the higher P_{att} and σ of CPS demonstrates that the wettability factor dominantly contributes to the interfacial attachment behavior, rather than the electrostatic factor. Consistently, APS particles have two favorable factors to the interfacial attachment such as the large contact angle ($\theta_c = 134.2 \pm 1.7^\circ$) and the weak electrostatic interaction, resulting in the highest P_{att} and σ among the three types of PS particles.

The proposed mechanism of particle attachment efficacy to the interface was summarized and further discussed in terms of wettability and interparticle interactions. For the wettability effect, the favorable condition for a stable attachment was the case of high θ_c , where particles reside more preferentially in the oil phase. When the particle solution, along with the spreading solvent, is added to the oil–water interface, strong convective flow occurs. This flow can provide energy for the particles adsorbed at the interface to detach from the interface. This flow-induced detachment phenomenon likely occurs more actively in the case of hydrophilic particles that prefer water (Fig. 7a and b). For the interparticle interaction effect, as depicted in Fig. 7c and d, strong electrostatic dipolar repulsion at lower salt concentrations prevents additional particle attachment to the interface. In this case, the effective diameter should be much larger than the particle diameter, which reduces the free interface area for additional particle attachment. In contrast, the local interface deformation-induced capillary force becomes dominant when the dipolar repulsion is significantly reduced at higher salt concentrations. The formation of aggregates and percolated network structures of interface-attached particles provides more space for particle adsorption.

4. Conclusion

We investigated the effects of interparticle interactions and wettability on the particle attachment efficacy to the oil–water interface. Three types of PS particles with different surface functional groups were examined at varying salt concentrations and the number of particles injected into the interface. Based on the microfluidic method and the surface coverage measurement, we found that the two contributing factors significantly influenced particle attachment efficiency to the interface, while the wettability factor has a major contribution. In our future studies, the complex interplay between other parameters, such as particle shape, particle size, particle mixture with heterogeneous sizes, oil phase thickness, and different types and amounts of spreading solvents, will be quantitatively evaluated via the developed microfluidic platform. Using a high-speed camera, we will also conduct a study to determine the critical force by which a particle in the oil phase with a spreading solvent can be transferred to the aqueous phase after colliding with the oil–water interface. We believe that this study deepens the understanding of fundamental physicochemical aspects in the assembly of particles at fluid interfaces and potentially provides engineering strategies for forming interfaces with tailored structures that would determine mechanical or rheological interfacial performances.

Author contribution statement

In Hwan Jung: Performed the experiments; Analyzed and interpreted the data; Wrote the paper.

Kyu Hwan Choi: Performed the experiments; Analyzed and interpreted the data.

Tae Seok Seo: Conceived and designed the experiments; Analyzed and interpreted the data; Contributed reagents, materials, analysis tools or data.

Hyosung An, Bum Jun Park: Conceived and designed the experiments; Analyzed and interpreted the data; Contributed reagents, materials, analysis tools or data; Wrote the paper.

Data availability statement

All data are presented in the paper. Any additional information can be obtained from corresponding authors upon request.

Declaration of competing interest

The authors declare that they have no known competing financial interests or personal relationships that could have appeared to influence the work reported in this paper.

Acknowledgements

This work was supported by the National Research Foundation (NRF) of Korea, No. NRF-2021R1A5A6002853 and NRF-2020R1A2B5B01001949. This work was also supported by the Korea Institute for Advancement of Technology (KIAT) and the Ministry of Trade, Industry & Energy (MOTIE) of the Republic of Korea (No. P0017363) and the Basic Research Capacity Enhancement Project through Korea Basic Science Institute (National Research Facilities and Equipment Center) grant funded by the Ministry of Education (No. 2019R1A6C101052).

References

- [1] E. Dickinson, Food emulsions and foams: stabilization by particles, *Curr. Opin. Colloid Interface Sci.* 15 (1–2) (2010) 40–49.
- [2] M. Rayner, D. Marku, M. Eriksson, M. Sjöö, P. Dejmek, M. Wahlgren, Biomass-based particles for the formulation of Pickering type emulsions in food and topical applications, *Colloids Surf. A Physicochem. Eng. Asp.* 458 (2014) 48–62.
- [3] M.S. Silverstein, PolyHIPEs: recent advances in emulsion-templated porous polymers, *Prog. Polym. Sci.* 39 (1) (2014) 199–234.
- [4] M. Marquis, V. Alix, I. Capron, S. Cuenot, A. Zykwincka, Microfluidic encapsulation of pickering oil microdroplets into alginate microgels for lipophilic compound delivery, *ACS Biomater. Sci. Eng.* 2 (4) (2016) 535–543.
- [5] J. Marto, A. Ascenso, S. Simoes, A.J. Almeida, H.M. Ribeiro, Pickering emulsions: challenges and opportunities in topical delivery, *Expert Opin. Drug Deliv.* 13 (8) (2016) 1093–1107.
- [6] J. Wu, G.H. Ma, Recent studies of Pickering emulsions: particles make the difference, *Small* 12 (34) (2016) 4633–4648.
- [7] K.Y. Yoon, H.A. Son, S.K. Choi, J.W. Kim, W.M. Sung, H.T. Kim, Core flooding of complex nanoscale colloidal dispersions for enhanced oil recovery by in situ formation of stable oil-in-water pickering emulsions, *Energy Fuels* 30 (4) (2016) 2628–2635.
- [8] D. Venkataramani, A. Tsulaia, S. Amin, Fundamentals and applications of particle stabilized emulsions in cosmetic formulations, *Adv. Colloid Interface Sci.* 283 (2020), 102234.
- [9] S.U. Pickering, CXCVI.—emulsions, *J. Chem. Soc. Trans.* 91 (1907) 2001–2021.
- [10] W. Ramsden, Separation of solids in the surface-layers of solutions and 'suspensions' (observations on surface-membranes, bubbles, emulsions, and mechanical coagulation), Preliminary account, *Proc. R. Soc. Lond.* 72 (477–486) (1904) 156–164.
- [11] H. Jiang, Y. Sheng, T. Ngai, Pickering emulsions: versatility of colloidal particles and recent applications, *Curr. Opin. Colloid Interface Sci.* 49 (2020) 1–15.
- [12] S. Crossley, J. Faria, M. Shen, D.E. Resasco, Solid nanoparticles that catalyze biofuel upgrade reactions at the water/oil interface, *Science* 327 (5961) (2010) 68–72.
- [13] F. Chang, C.M. Vis, W. Ciptonugroho, P.C. Bruijninx, Recent developments in catalysis with Pickering emulsions, *Green Chem.* 23 (7) (2021) 2575–2594.
- [14] B. Seo, M. Sung, B.J. Park, J.W. Kim, Recyclable 2D colloid surfactants with high catalytic activities at pickering emulsion interfaces, *Adv. Funct. Mater.* 32 (17) (2022), 2110439.
- [15] B.J. Park, D. Lee, Particles at fluid–fluid interfaces: from single-particle behavior to hierarchical assembly of materials, *MRS Bull.* 39 (12) (2014) 1089–1098.
- [16] B.P. Binks, Particles as surfactants—similarities and differences, *Curr. Opin. Colloid Interface Sci.* 7 (1–2) (2002) 21–41.
- [17] H.H. Wickman, J.N. Korley, Colloid crystal self-organization and dynamics at the air/water interface, *Nature* 393 (6684) (1998) 445–447.
- [18] A. Stocco, E. Rio, B.P. Binks, D. Langevin, Aqueous foams stabilized solely by particles, *Soft Matter* 7 (4) (2011) 1260–1267.
- [19] S. Barman, G.F. Christopher, Simultaneous interfacial rheology and microstructure measurement of densely aggregated particle laden interfaces using a modified double wall ring interfacial rheometer, *Langmuir* 30 (32) (2014) 9752–9760.
- [20] S.C. Glotzer, M.J. Solomon, Anisotropy of building blocks and their assembly into complex structures, *Nat. Mater.* 6 (8) (2007) 557–562.
- [21] A. Maestro, E. Santini, E. Guzmán, Physico-chemical foundations of particle-laden fluid interfaces, *Eur. Phys. J. E* 41 (2018) 1–21.
- [22] L. Botto, E.P. Lewandowski, M. Cavallaro, K.J. Stebe, Capillary interactions between anisotropic particles, *Soft Matter* 8 (39) (2012) 9957–9971.
- [23] J.-C. Loudet, A.M. Alsayed, J. Zhang, A.G. Yodh, Capillary interactions between anisotropic colloidal particles, *Phys. Rev. Lett.* 94 (2005), 018301.
- [24] K.H. Choi, D.W. Kang, S. Yoo, S. Lee, B.J. Park, Interpretation of electrostatic self-potential measurements using interface-trapped microspheres with surface heterogeneity, *ACS Appl. Polym. Mater.* 2 (3) (2020) 1304–1311.
- [25] J.H. Lim, J.Y. Kim, D.W. Kang, K.H. Choi, S.J. Lee, S.H. Im, B.J. Park, Heterogeneous capillary interactions of interface-trapped ellipsoid particles using the trap-release method, *Langmuir* 34 (1) (2018) 384–394.
- [26] M. Oettel, S. Dietrich, Colloidal interactions at fluid interfaces, *Langmuir* 24 (4) (2008) 1425–1441.
- [27] B.J. Park, T. Brugarolas, D. Lee, Janus particles at an oil–water interface, *Soft Matter* 7 (14) (2011) 6413–6417.
- [28] B.J. Park, C.-H. Choi, S.-M. Kang, K.E. Tetty, C.-S. Lee, D. Lee, Geometrically and chemically anisotropic particles at an oil–water interface, *Soft Matter* 9 (12) (2013) 3383–3388.
- [29] B.J. Park, C.-H. Choi, S.-M. Kang, K.E. Tetty, C.-S. Lee, D. Lee, Double hydrophilic Janus cylinders at an air–water interface, *Langmuir* 29 (6) (2013) 1841–1849.
- [30] A.J. Hurd, The electrostatic interaction between interfacial colloidal particles, *J. Phys. A* 18 (16) (1985) L1055.
- [31] D. Stamou, C. Duschl, D. Johannsmann, Long-range attraction between colloidal spheres at the air-water interface: the consequence of an irregular meniscus, *Phys. Rev. E* 62 (4) (2000) 5263.
- [32] H. Rezvantalab, S. Shojaei-Zadeh, Capillary interactions between spherical Janus particles at liquid–fluid interfaces, *Soft Matter* 9 (13) (2013) 3640–3650.
- [33] P. Pieranski, Two-dimensional interfacial colloidal crystals, *Phys. Rev. Lett.* 45 (7) (1980) 569.
- [34] B.J. Park, D. Lee, Equilibrium orientation of nonspherical Janus particles at fluid–fluid interfaces, *ACS Nano* 6 (1) (2012) 782–790.
- [35] B.J. Park, D. Lee, Configuration of nonspherical amphiphilic particles at a fluid–fluid interface, *Soft Matter* 8 (29) (2012) 7690–7698.
- [36] T.G. Anjali, M.G. Basavaraj, Contact angle and detachment energy of shape anisotropic particles at fluid–fluid interfaces, *J. Colloid Interface Sci.* 478 (2016) 63–71.
- [37] B.P. Binks, T.S. Horozov, *Colloidal Particles at Liquid Interfaces*, Cambridge University Press, 2006.
- [38] E. Guzmán, I. Abelenda-Núñez, A. Maestro, F. Ortega, A. Santamaria, R.G. Rubio, Particle-laden fluid/fluid interfaces: physico-chemical foundations, *J. Phys. Condens. Matter* 33 (33) (2021), 333001.

- [39] E. Guzmán, F. Martínez-Pedrero, C. Calero, A. Maestro, F. Ortega, R.G. Rubio, A broad perspective to particle-laden fluid interfaces systems: from chemically homogeneous particles to active colloids, *Adv. Colloid Interface Sci.* (2022), 102620.
- [40] E. Guzmán, F. Ortega, R.G. Rubio, Forces controlling the assembly of particles at fluid interfaces, *Langmuir* 38 (44) (2022) 13313–13321.
- [41] T. Ngai, S.A. Bon, *Particle-stabilized Emulsions and Colloids: Formation and Applications*, Royal society of chemistry, 2014.
- [42] D. Zang, E. Rio, G. Delon, D. Langevin, B. Wei, B. Binks, Influence of the contact angle of silica nanoparticles at the air–water interface on the mechanical properties of the layers composed of these particles, *Mol. Phys.* 109 (7–10) (2011) 1057–1066.
- [43] A. Maestro, L.J. Bonales, H. Ritacco, T.M. Fischer, R.G. Rubio, F. Ortega, Surface rheology: macro-and microrheology of poly (tert-butyl acrylate) monolayers, *Soft Matter* 7 (17) (2011) 7761–7771.
- [44] F. Ortega, H. Ritacco, R.G. Rubio, Interfacial microrheology: particle tracking and related techniques, *Curr. Opin. Colloid Interface Sci.* 15 (4) (2010) 237–245.
- [45] S. Reynaert, P. Moldenaers, J. Vermant, Control over colloidal aggregation in monolayers of latex particles at the oil–water interface, *Langmuir* 22 (11) (2006) 4936–4945.
- [46] B.J. Park, E.M. Furst, Attractive interactions between colloids at the oil–water interface, *Soft Matter* 7 (17) (2011) 7676–7682.
- [47] B.J. Park, J.P. Pantina, E.M. Furst, M. Oettel, S. Reynaert, J. Vermant, Direct measurements of the effects of salt and surfactant on interaction forces between colloidal particles at water–oil interfaces, *Langmuir* 24 (5) (2008) 1686–1694.
- [48] V.N. Paunov, Novel method for determining the three-phase contact angle of colloid particles adsorbed at air–water and oil–water interfaces, *Langmuir* 19 (19) (2003) 7970–7976.
- [49] H.W. Jeong, J.W. Park, H.M. Lee, K.H. Choi, S.J. Lee, J.W. Kim, B.J. Park, Retardation of capillary force between janus particles at the oil–water interface, *J. Phys. Chem. Lett.* 13 (42) (2022) 10018–10024.
- [50] C.A. Schneider, W.S. Rasband, K.W. Eliceiri, NIH Image to ImageJ: 25 years of image analysis, *Nat. Methods* 9 (7) (2012) 671–675.
- [51] K.C. Neuman, S.M. Block, Optical trapping, *Rev. Sci. Instrum.* 75 (2004) 2787–2809.
- [52] A.B. Hopkins, F.H. Stillinger, S. Torquato, Densest local sphere-packing diversity: general concepts and application to two dimensions, *Phys. Rev. E* 81 (4) (2010), 041305.
- [53] J.I. Shin, S.J. Cho, J. Jeon, K.H. Lee, J.J. Wie, Three-dimensional micropatterning of semiconducting polymers via capillary force-assisted evaporative self-assembly, *Soft Matter* 15 (19) (2019) 3854–3863.